Downfront Winds over Buoyant Coastal Plumes

MICHAEL A. SPALL

Woods Hole Oceanographic Institution, Woods Hole, Massachusetts

LEIF N. THOMAS

Department of Earth System Science, Stanford University, Stanford, California

(Manuscript received 15 February 2016, in final form 8 August 2016)

ABSTRACT

Downfront, or downwelling favorable, winds are commonly found over buoyant coastal plumes. It is known that these winds can result in mixing of the plume with the ambient water and that the winds influence the transport, spatial extent, and stability of the plumes. In the present study, the interaction of the Ekman velocity in the surface layer and baroclinic instability supported by the strong horizontal density gradient of the plume is explored with the objective of understanding the potential vorticity and buoyancy budgets. The approach makes use of an idealized numerical model and scaling theory. It is shown that when winds are present the weak stratification resulting from vertical mixing and the strong baroclinicity of the front results in near-zero average potential vorticity q. For weak to moderate winds, the reduction of q by diapycnal mixing is balanced by the generation of q through the geostrophic stress term in the regions of strong horizontal density gradients and stable stratification. However, for very strong winds the wind stress overwhelms the geostrophic stress and leads to a reduction in q, which is balanced by the vertical mixing term. In the absence of winds, the geostrophic stress dominates mixing and the flow rapidly restratifies. Nonlinearity, extremes of relative vorticity and vertical velocity, and mixing are all enhanced by the presence of a coast. Scaling estimates developed for the eddy buoyancy flux, the surface potential vorticity flux, and the diapycnal mixing rate compare well with results diagnosed from a series of numerical model calculations.

1. Introduction

Downwelling-favorable winds are often found over buoyant coastal plumes. For example, the surface waters along the east coast of Greenland are buoyant due to the relatively fresh waters coming out of the Arctic Ocean and freshwater runoff from glacial melt over Greenland and are exposed to strong winds. The fate of these buoyant waters is of particular concern because it has been hypothesized that if this water were able to get off the shelf and into the open ocean, the surface waters could become sufficiently buoyant as to shut down deep convection (Dickson et al. 1988). This has implications for the global-scale meridional overturning circulation and meridional heat and freshwater transports (Fichefet et al. 2003; Jungclaus et al. 2006). Barrier wind events with downwelling-favorable winds exceeding $20\,\mathrm{m\,s^{-1}}$, with surface wind stresses between 0.5 and $1\,\mathrm{N\,m^{-2}}$, commonly occur in winter along the east coast of Greenland (Harden et al. 2011). The role of winds in mixing and advecting these waters along the coast is thus of interest. There are many other examples of recurring downwelling-favorable coastal winds, albeit much less dramatic. Such winds in the western Mediterranean intensify instabilities and biological productivity in buoyant fronts along the Spanish coast (Oguz et al. 2015). On the Atlantic coast of France, downwelling-favorable winds in the Bay of Biscay force poleward buoyant boundary currents derived from the Gironde and Adour River outflows (Batifoulier et al. 2012). Similar buoyant coastal plumes are found throughout the World Ocean, so the question of how these plumes respond to downwelling-favorable winds in terms of mixing and ageostrophic circulations (and the potential nutrient supply to the euphotic zone) is a general and important one.

Many previous modeling studies of downwelling-favorable winds have been in two dimensions and/or idealized domains. Allen and Newburger (1996) showed that downwelling-favorable winds lead to the formation

Corresponding author address: Michael Spall, MS 21, 360 Woods Hole Road, Woods Hole, MA 02543.
E-mail: mspall@whoi.edu

DOI: 10.1175/JPO-D-16-0042.1

© 2016 American Meteorological Society

of a well-mixed water mass in the inshore region and a strong front at the transition from coastal to offshore waters and that the flow was susceptible to symmetric instabilities in the bottom boundary layer. Moffat and Lentz (2012) provided analytic and scaling estimates for the width, transport, and mixing in buoyant coastal plumes subject to downwelling-favorable winds. They also showed that the cross-shelf circulation can be reversed from the expected Ekman transport if the density gradient across the front is sufficiently large due to the stress induced by the geostrophic shear.

There have also been numerous realistic numerical model configurations used to study the impact of downwelling-favorable winds on buoyant coastal plumes. Whitney and Garvine (2005) derive and test a scaling for the relative importance of wind versus buoyancy for the Delaware Coastal Current and show that for realistic wind events the wind forcing can dominate the flow. Using realistic and idealized numerical models, Magaldi et al. (2010) showed that downwelling-favorable winds over the West Adriatic Current (along the east coast of Italy) intensify and stabilize the current and also induce mixing that dilutes the freshwater plume.

For buoyant coastal currents, downwelling-favorable winds are downfront, that is, they are aligned with the thermal wind shear and hence induce frictional potential vorticity (PV) fluxes that lower the potential vorticity of the current (Thomas 2005). Physically, downfront winds drive Ekman flows that advect water from the dense side of fronts over lighter waters, reducing the stratification and potential vorticity in the surface boundary layer. This makes fronts susceptible to submesoscale instabilities such as symmetric and mixed layer baroclinic instability (Thomas and Taylor 2010; Boccaletti et al. 2007). Both types of instabilities restratify the surface boundary layer via cross-front overturning circulations that counteract the destratifying Ekman flow (D'Asaro et al. 2011; Fox-Kemper et al. 2008; Mahadevan et al. 2010). Studies of submesoscale instabilities forced by downfront winds and their potential vorticity dynamics have focused on open-ocean applications. With a coast, downfront wind forcing sets up a large-scale frontogenetic flow that likely complicates the potential vorticity dynamics of the submesoscale instabilities that result.

There already has been much work done on downwelling-favorable, or downfront, winds along the coast and the few studies mentioned above demonstrate the wide-ranging geographical extent of this problem. However, most of this work has been aimed at describing the evolution of the isopycnals and understanding the characteristics of the flow (width, depth, transport, and stratification). There has been much less focus on the interaction of the Ekman transport with the ageostrophic flows resulting from baroclinic instability of the front, the potential vorticity dynamics of the flow, or on the mechanisms and rate of water mass transformation driven by the combination of eddy fluxes and winds. The present study takes a very idealized approach to describe the quasi-steady balances of momentum, buoyancy, and potential vorticity and to develop scaling estimates for potential vorticity fluxes, eddy fluxes, and the water mass transformation rate.

2. Numerical configuration

An idealized numerical model is used to explore the response of a buoyant coastal plume to downfront winds. The model is the hydrostatic primitive equation Massachusetts Institute of Technology General Circulation Model (MITgcm; Marshall et al. 1997). Most calculations are in a periodic channel 100 km in both zonal and meridional extent. All calculations are on an f plane with $f_0 = 10^{-4}\,\mathrm{s}^{-1}$, but for discussion purposes increasing y will be referred to as north and increasing x is east. The boundary conditions are periodic in the north–south direction with solid walls at $x = 0$ and 100 km. There is a sloping bottom that goes from 10 m at $x = 0$ to 100 m at $x = 90$ km (bottom slope 0.001). The model uses the KPP mixing scheme in the vertical (Large et al. 1994), a quadratic bottom drag with coefficient 0.0025, a Smagorinsky lateral Laplacian viscosity with nondimensional coefficient $C = 2.5$, and free-slip lateral boundary conditions. The boundary conditions for salinity are no flux through all boundaries (side, bottom, and surface). There is no explicit horizontal diffusion of salinity, although the numerical advection scheme does have some implicit mixing (quantified below). The background Laplacian vertical diffusion is $10^{-5}\,\mathrm{m}^2\,\mathrm{s}^{-1}$ for both salinity and momentum. The horizontal grid spacing is 500 m, and the vertical grid spacing is 2 m.

The model momentum equation is written as

$$\mathbf{u}_t + \mathbf{u}\cdot\nabla\mathbf{u} + f_0\mathbf{k}\times\mathbf{u} = -\nabla\phi/\rho_0 + \mathbf{F}, \tag{1}$$

where $\mathbf{F}$ represents the mixing of momentum by vertical viscosity κ_v with the coefficient calculated by the KPP parameterization, horizontal viscosity with the Smagorinsky parameterization, and quadratic bottom drag. The hydrostatic pressure is given by ϕ, ρ_0 is a reference density, and $\mathbf{k}$ is the unit vertical vector. Subscripts indicate partial differentiation.

The model salinity equation is written as

$$S_t + \nabla\cdot(\mathbf{u}S) = (\kappa_S S_z)_z = D_S. \tag{2}$$

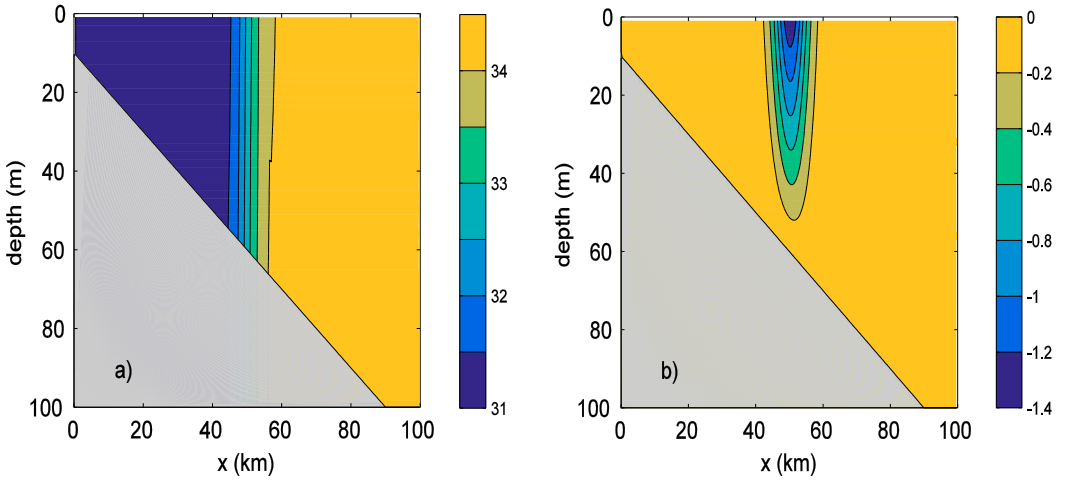

FIG. 1. Initial profile for (a) salinity (psu) and (b) meridional velocity ($\mathrm{m\,s^{-1}}$).

The only mixing explicitly represented in the salinity equation is through vertical diffusion with the coefficient κ_S calculated from KPP, written for convenience as D_S.

The initial salinity profile has freshwater with $S = 31$ psu over the shallow slope and salty water with $S = 34$ psu over the deep slope, giving a change in salinity across the front of $\Delta S = 3$ psu, with a hyperbolic tangent transition at $x = 50$ km with horizontal scale of 10 km (Fig. 1). A linear equation of state is used with a haline contraction coefficient of $\alpha_S = 0.8\,\mathrm{kg\,m^{-3}\,psu^{-1}}$, so the change in buoyancy $b(=-g\rho/\rho_0)$ across the front is $\Delta b = -g\alpha_S \Delta S/\rho_0 = -0.023\,\mathrm{m\,s^{-2}}$. This is an approximation of a two-layer system with a fresh, buoyant plume along the coast. The initial velocity field is in geostrophic balance with zero velocity at the bottom. This gives a maximum southward velocity of approximately $1.4\,\mathrm{m\,s^{-1}}$ at the surface. This is similar to the equilibrium state derived by Moffat and Lentz (2012) for two-dimensional downwelling conditions. The model could instead have been initialized with a motionless flow field and uniformly stratified flow. The subsequent downwelling-favorable winds would lead to steepening of the isopycnals and an acceleration of a southward flow, similar to that used for initialization here. This approach was not taken because there was found to be significant mixing induced during the spinup phase, which makes identifying the equilibrium balances as a function of the initial salinity difference across the front much more difficult.

The central model calculation discussed in detail below is forced with a uniform meridional wind stress of $\tau = -0.2\,\mathrm{N\,m^{-2}}$ that is ramped up with a hyperbolic tangent function over the first week of integration and then held constant. The model is run for 20 days, and most of the analysis is taken between days 10 and 20. By day 10 the wind is at full strength and the front has a sufficient time to develop baroclinic instabilities.

3. Mean balances

The time and meridionally averaged mean properties are shown in Fig. 2. The salinity gradient is now greatly reduced, although the change in salinity between the onshore and offshore boundaries remains the same as in the initial conditions. The strongest gradient is found at the surface near $x = 60$ km. The mean front is also weakly stratified in the center of the domain. The mean meridional velocity is surface intensified with maximum southward flow of approximately $0.75\,\mathrm{m\,s^{-1}}$. There is now a strong barotropic component that is everywhere toward the south but decreases near the bottom in the bottom boundary layer. The spinup time for this barotropic response is rapid and scales as $h/(4C_d|\tau|/\rho_0)^{1/2} \approx 0.5$ days for a depth of $h = 50$ m and a wind stress magnitude of $|\tau| = 0.2\,\mathrm{N\,m^{-2}}$. The zonal velocity is onshore in the upper part of the water column and offshore near the bottom. This is broadly consistent with the expected Ekman transports in the surface and bottom boundary layers. The maximum onshore and offshore velocities are found near $x = 50$ km. This is where the mean relative vorticity is anticyclonic, which causes an increase in the Ekman transport because it is inversely proportional to the absolute vorticity $f_0 + \zeta$, where $\zeta = v_x - u_y$ is the relative vorticity (Stern 1965; Niiler 1969). The onshore transport weakens for depths less than 30 m due to the overlap between the surface and bottom boundary layers.

Sections of the mean balance in the meridional momentum equation support this simple interpretation (not shown). The dominant balance is between viscosity and the Coriolis term, which is given by f_0 times the

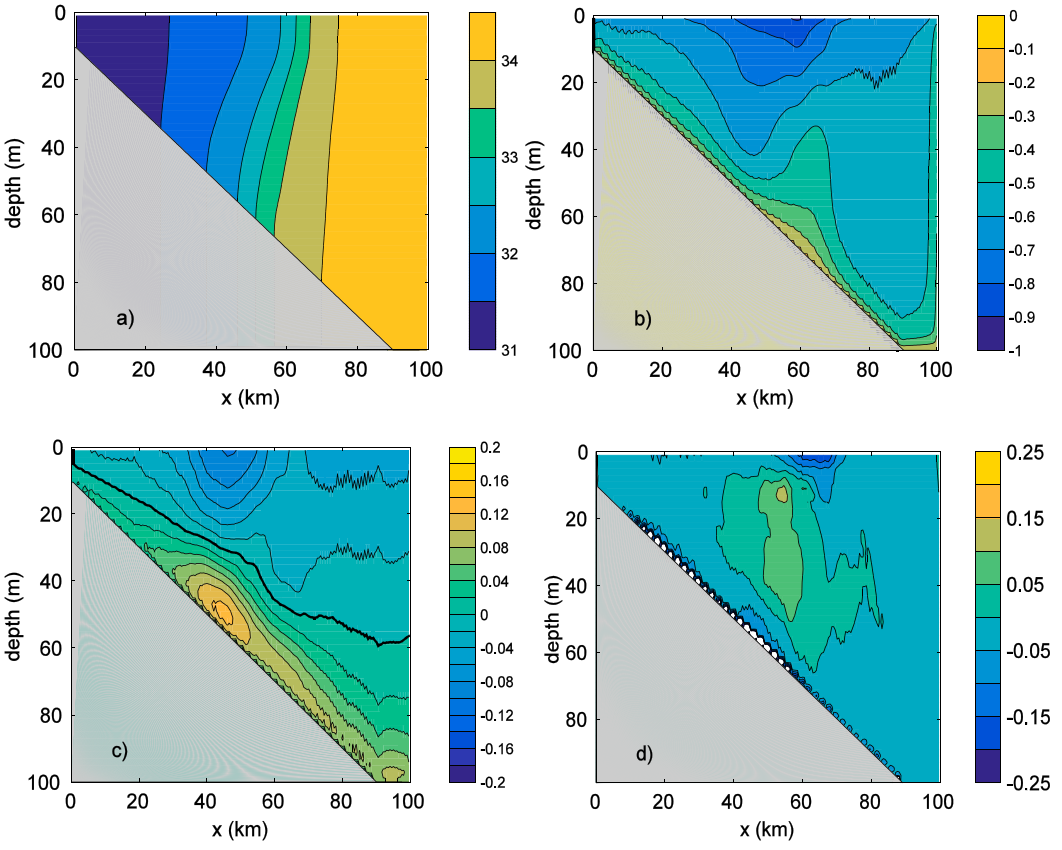

FIG. 2. Time-mean sections between days 10 and 20 for (a) salinity (psu), (b) meridional velocity (m s^{-1}), (c) zonal velocity (m s^{-1}; zero contour is thick), and (d) Ertel potential vorticity q (10^{-7} s^{-3}) for run 1 in Table 1.

zonal velocity in Fig. 2c, with only a minor contribution due to advection of relative vorticity near the region of strong cyclonic vorticity at the surface.

The Ertel potential vorticity q (Hoskins 1974) is defined as

$$q = (f_0 + \zeta)b_z + (u_z - w_x)b_y + (w_y - v_z)b_x. \qquad (3)$$

The mean potential vorticity is negative near the surface and bottom and positive at middepths in the frontal region (Fig. 2d). In the frontal region, the mean q is dominated by the $f_0 b_z$ term.

Sections of the mean terms in the salinity equation are shown in Fig. 3. The balance is between advection making the surface fresher and vertical diffusion making the surface saltier. This is not what would be expected if the balance were vertical mixing balancing the onshore Ekman transport at the surface. In that balance, advection would be making the surface saltier in the frontal zone and vertical mixing would be making it fresher (by mixing salty water down and freshwater up). The advection term is decomposed into mean and time-dependent contributions, that is, $-\overline{\nabla \cdot (\mathbf{u}S)} = -\overline{\mathbf{u}} \cdot \nabla \overline{S} - \nabla \cdot (\overline{\mathbf{u}'S'})$, where $\overline{(\,)}$ denotes a time average and primes indicate the deviation from that average. It is found that the mean advection is working to make the surface saltier and the near bottom fresher, just as would be expected for the destabilizing Ekman transport. However, the time-dependent contribution is of opposite sign and larger, especially near the surface, so it dominates the advective contribution. The eddy flux shown here is calculated from the full three component velocity field, but it is dominated by the horizontal eddy fluxes. Near the bottom, the mean and advection terms nearly cancel, resulting in relatively weak mixing in the bottom boundary layer. Vertical diffusion near the surface modifies the salinity and so leads to water mass transformation. However, it is not because dense water is being advected over light water by the Ekman transport but because eddies are restratifying the surface layer and mechanical energy put in by the wind is mixing downward working to remove the stratification.

4. Dynamics and water mass transformation

One of the primary objectives of this study is to understand what drives the mixing and water mass

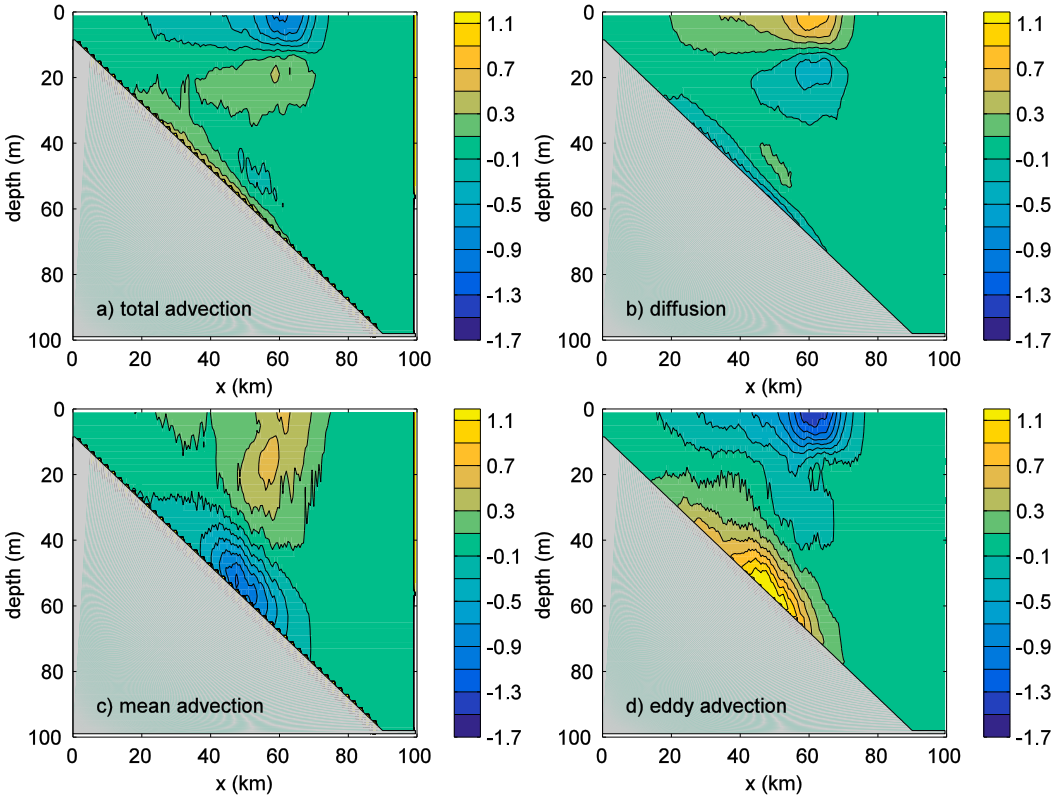

FIG. 3. Mean terms in the salinity budget (10^{-5} psu s^{-1}) between days 10 and 20 for (a) total advection, (b) diffusion, (c) mean advection, and (d) eddy advection for run 1.

transformation depicted in Fig. 3b. To do this, it is instructive to first consider the dynamical balances in the regions of mixing. A snapshot of the sea surface salinity on day 15 is shown in Fig. 4a. The surface is dominated by a sharp, meandering front with long filaments that extend toward the coast. The dominant meander length is approximately 35 km, so about three meanders are represented at any one time. This is typical of the sea surface salinity for all times after about 10 days.

The planetary boundary layer thickness δ is shown in Fig. 4b. The boundary layer thickness is a Richardson number–based diagnostic quantity provided by the KPP mixing scheme as the depth to which mixing penetrates and is generally slightly deeper than the depth of weak stratification. The boundary layer thickness is relatively shallow, $O(25)$ m, in the frontal region where salinity transitions from fresh to salty. Onshore and offshore of this region, the boundary layer thickness extends all the way to the bottom.[1] The transition from a shallow boundary layer to a deep boundary layer can be very abrupt, spanning only a few kilometers or less. The regions of stratification are very patchy and punctuated by deeper boundary layers along the high-salinity filaments that extend shoreward.

The time rate of change of sea surface salinity due to vertical mixing, evaluated at the surface, is shown in Fig. 4c. The mixing is small over most of the domain but large and positive (increasing surface salinity) in the frontal regions, especially so along the northern edge of the filaments. The mixing is slightly negative (decreasing surface salinity) on the southern (or downstream) side of the filaments, indicating that the vertical density gradient is positive in these regions. This results from the strong southward flow driven by the downfront winds advecting the upper portions of the dense, salty filaments over the fresher water to the south. However, there is clearly an asymmetry in the north–south direction such that the regions of increasing salinity are larger and have stronger mixing than the regions of decreasing salinity. Similar strength mixing is seen independent of the meander orientation, so it does not appear to be directly related to the direction of the Ekman transport.

[1] The bottom depth is evident by the straight contours.

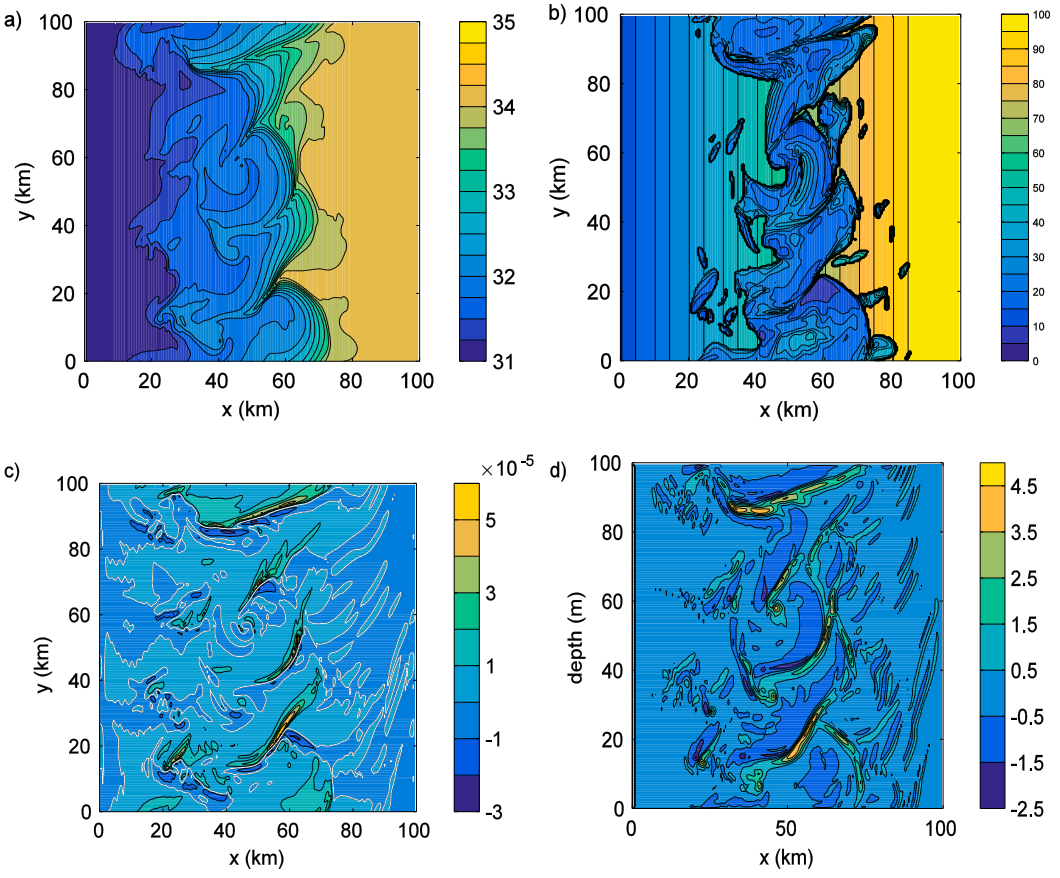

FIG. 4. Snapshot on day 15 from run 1 of (a) sea surface salinity (psu), (b) planetary boundary layer thickness δ (m), (c) time rate of change of surface salinity due to vertical mixing (psu s^{-1}; zero contour is white), and (d) relative vorticity divided by f_0.

The relative vorticity normalized by f_0 is shown in Fig. 4d. The filaments are regions of intense positive ($>4f_0$) and negative ($<-f_0$) relative vorticity. As will be shown below, the water mass transformation at the surface due to vertical mixing takes place primarily in the regions of negative relative vorticity.

Further evidence that the mixing is not simply a result of the Ekman transport advecting dense water over light water comes from a volumetric census of salinity at the beginning and end of the integration. As shown in Fig. 5, a probability density function (pdf) of the initial salinity distribution is dominated by two modes, one at 31 psu and one at 34 psu (thin black line). The salinity on day 20 shows that the fresh mode has been significantly eroded away and a product water of intermediate salinity has been formed. This was caused by the mixing of the freshwater with the salty water below shown in Fig. 4c (there is also a reduction in the volume of salty water, but it is not as clear in the figure because of the large initial volume). An identical calculation in two dimensions shows very little change in salinity over the course of integration (blue line). There is a slight increase in intermediate salinities, but it does not produce the mode water found in the three-dimensional case. The explanation for this weak net transformation is straightforward. The isohalines are nearly vertical, so that the offshore gradient of salinity is independent of depth. The onshore Ekman transport near the surface is balanced by the offshore Ekman transport near the bottom. So an integral of the advective salt flux divergence in a control volume defined by two isohalines is zero. Vertical mixing brings the salty water down and the freshwater up so that mixing balances lateral advection in both Ekman layers, resulting in little net transformation. Since there is no flux through the model boundaries, eventually even this slight mixing will result in a homogeneous water mass, but the time scale to achieve this mixing is much longer than the inherent dynamical time scales of the problem.

A three-dimensional case without wind is baroclinically unstable but also produces much less water mass

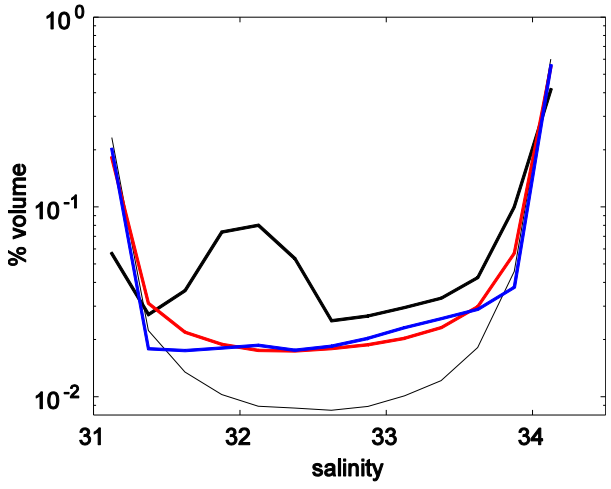

FIG. 5. Volumetric distribution of salinity for initial condition (thin black) and final state for three-dimensional with wind (run 1; thick black), two-dimensional with wind (blue), and three-dimensional without wind (red).

transformation (red line). If there were no numerical mixing due to the advection scheme and diapycnal mixing due to the background mixing could be neglected, then this case would have conserved the volumetric census from the initial state, so this is a measure of the nonconservative properties of the model configuration. There is slightly more mixing than for the two-dimensional case with wind, but still much less than the reference case. The large water mass transformation is not due solely to the destabilizing Ekman flow or baroclinic instability but results from the presence of both.

The water mass transformation rate S^* is defined as the volume integral of the time rate of change of salinity due to vertical mixing only in regions where salinity is increasing:

$$S^* = \iiint \mathcal{H}(D_S) D_S \, dx \, dy \, dz \,. \tag{4}$$

The Heaviside step function $\mathcal{H}(D_S)$ is one for $D_S > 0$ and zero for $D_S < 0$. This is the rate at which freshwater is being made salty. Of course the integral of the diapycnal mixing rate over the whole volume is zero since there is no buoyancy flux through the boundaries of the model, so we take the positive mixing regions as an indication of the strength of the water mass transformation. The vertical integral is either over the surface level only (Fig. 6) or over the full depth of the domain (Fig. 14d).

A census of the water mass transformation rate at the surface as a function of planetary boundary layer thickness and relative vorticity is shown in Fig. 6. Approximately 2/3 of the surface transformation takes place where the boundary layer thickness is less than 30 m. In addition, most of the transformation also takes place where the magnitude of the relative vorticity is between $-f_0$ and 0 or on the anticyclonic side of fronts, as suggested in Figs. 4c and 4d. The transformation is also predominantly in regions of upwelling (not shown).

Mixing is acting to reduce the stratification, and advection is acting to restratify the surface layer in the vicinity of the meanders, strong fronts, and filaments. The ageostrophic velocity on the anticyclonic side of the front is generally directed toward the front and increases in strength as the front is approached (Fig. 7a). This gives rise to upwelling of freshwater and a restratification by the ageostrophic velocity. The ageostrophic velocity changes abruptly as the front is crossed

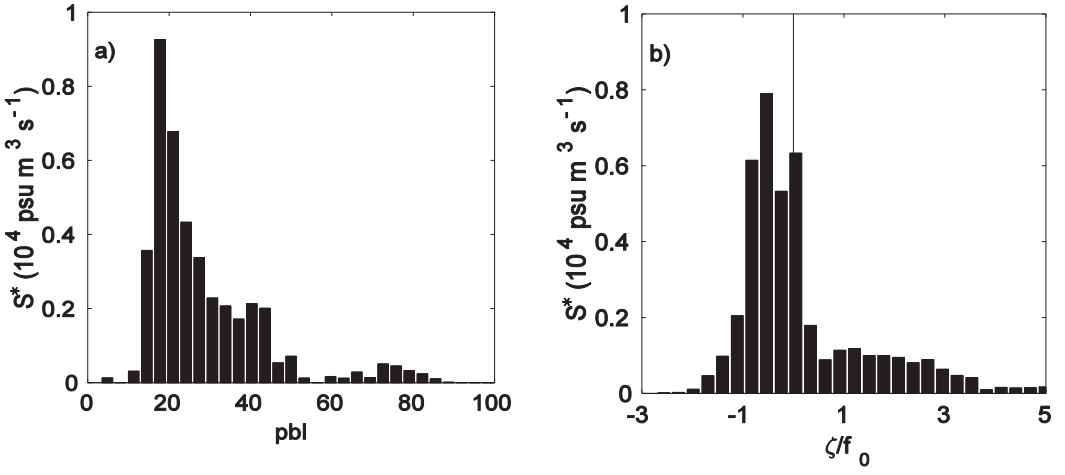

FIG. 6. Histogram of water mass transformation rate at the surface vs (a) planetary boundary layer thickness and (b) relative vorticity at the surface for run 1.

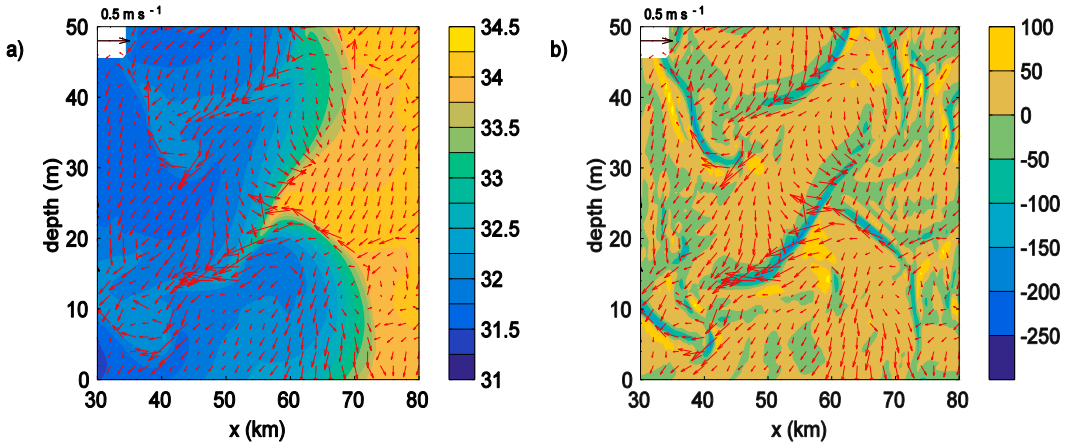

FIG. 7. Snapshot on model day 15 of (a) surface salinity (color) and (b) vertical velocity at 12-m depth (m day^{-1}) in a subregion of the domain for run 1. Ageostrophic velocity (vectors) is superimposed on both panels. A scale vector of 0.5 m s^{-1} is indicated by the black arrow in the upper-left corner of each panel.

from fresh to salty water. This is a region of intense downwelling of dense water (Fig. 7b). Such a stratifying ageostrophic circulation in the vicinity of a deformation field and intensifying front is expected from the theory of frontogenesis (Hoskins 1982) and is also consistent with frictional spindown (Thomas and Ferrari 2008).

The sharp gradients in the ageostrophic velocity are responsible for the narrow regions of intense downwelling. These transitions also coincide with gradients in the planetary boundary layer thickness and vertical mixing coefficient (not shown). Gradients in the filaments are weaker but show a local maximum in boundary layer thickness in the center of the dense plume. This filament structure is very similar to that described by McWilliams et al. (2015) and Gula et al. (2014). They used realistic and idealized numerical model calculations, along with an analytic theory, to describe the frontogenesis resulting from spatial variability in turbulent mixing, a process they call turbulent thermal wind (TTW). This drives frontogenesis and downwelling in the vicinity of dense filaments as is found here, a phenomenon that has also been derived in two-dimensional theoretical calculations (e.g., Garrett and Loder 1981; Thompson 2000; Nagai et al. 2006).

The combined influence of wind and baroclinic instability also strongly influences the occurrence of extreme vorticity and vertical motions. A pdf of relative vorticity and vertical velocity, averaged between days 10 and 20, is shown in Fig. 8. The case with both wind and baroclinic instability (black lines) produces much larger extremes of relative vorticity and vertical velocity than either wind or baroclinic instabilities alone. There is an asymmetry such that there are more strong positive relative vorticity and downwelling events than strong negative and upwelling, as expected. For the two-dimensional case, the relative

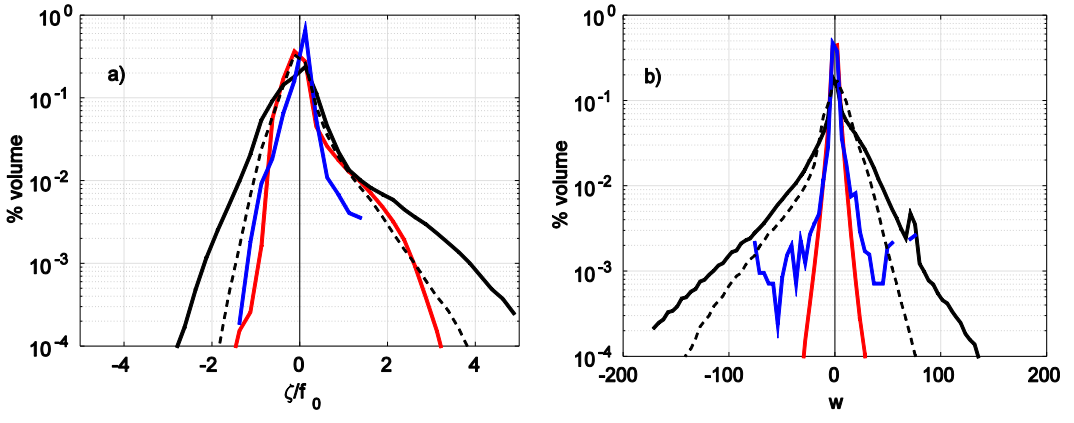

FIG. 8. Percentage distribution of (a) relative vorticity at the surface and (b) vertical velocity at 12-m depth (m day^{-1}). Black indicates three-dimensional with wind, blue indicates two-dimensional with wind, red indicates three-dimensional without wind, and dashed indicates three-dimensional with wind and without coast.

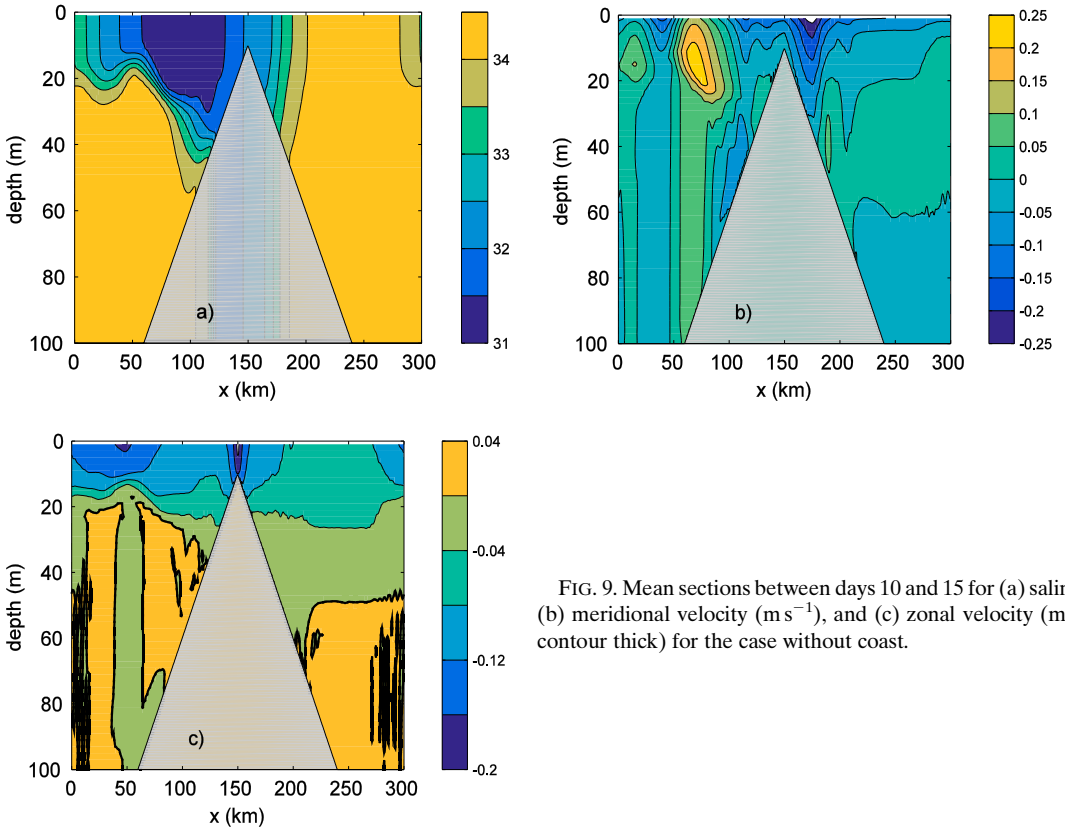

FIG. 9. Mean sections between days 10 and 15 for (a) salinity (psu), (b) meridional velocity ($m\,s^{-1}$), and (c) zonal velocity ($m\,s^{-1}$; zero contour thick) for the case without coast.

vorticity never exceeds $2f_0$ and the vertical velocity is generally less than $50\,m\,day^{-1}$. The relative vorticity for the three-dimensional case without wind is rarely less than $-f_0$, which is as expected with no surface forcing to destabilize the flow. There are more extreme positive relative vorticity events, but they still do not match the wind-forced case. The extreme vertical velocity events are much less frequent than for either case with wind forcing.

a. Comparison with open-ocean downfront winds

There are a number of differences between the case of downfront winds in the coastal region and downfront winds in the open ocean. While most previous studies of open-ocean downfront winds have neglected bottom topography, the cleanest way to demonstrate the influence of the coast is to retain the bottom topography and simply replace the vertical wall at the western and eastern boundaries with a periodic boundary condition. To make the initial conditions periodic, the topography and initial salinity field are reflected across the shallowest topography, which is now in the middle of the domain.

The salinity averaged in the meridional direction between days 10 and 15 is shown in Fig. 9a. The freshwater that was initially over shallow water has been advected to the west by the Ekman transport. Since the Ekman transport is strongest at the surface, the flow to the west of the ridge is being strongly stratified (upfront wind), while the flow to the east of the ridge is weakly stratified. The meridional velocity (Fig. 9b) is quite different from the case with a coast. The southward flow over the eastern slope is weaker, both in terms of the vertical shear and the barotropic velocity (note the difference in color scale with Fig. 2b). There is also no strong vertical shear near the bottom because the near-bottom velocity, and thus the bottom Ekman layer, is weak. The zonal velocity is westward over most of the water column (Fig. 9c). The surface Ekman layer penetrates deeper to the east of the ridge than to the west because of the difference in stratification. The Ekman velocity is increased over shallow water as the Ekman transport is squeezed through the 10-m-deep passage. The momentum budget is consistent with a linear Ekman layer balance; the nonlinear advection of relative vorticity is small. It is evident from comparing Figs. 9a and 2a that most of the low-salinity water is simply advected to the west when there is no coast, while it is trapped over shallow water when the coast is present.

Extreme relative vorticity events are at least an order of magnitude less common with no coast, and negative relative vorticities exceeding $-2f_0$ are not found (Fig. 8,

dashed line). There are also many fewer extreme vertical velocity events with no coastline.

Each of these differences between the no coast case and the coast case is a result of the no-normal flow boundary condition at the coast. This causes the sea surface height to build up due to the onshore Ekman transport. This results in a zonal gradient in sea surface height, which is balanced by a strong barotropic flow to the south. This acceleration is halted by the development of a bottom boundary layer that is able to transport an equivalent amount of water offshore to close the zonal circulation. The overlap of the surface and bottom boundary layers essentially isolates the near-coast water from the rest of the domain and results in a large-scale frontogenetic configuration with onshore Ekman transport at the surface, offshore at the bottom, and no zonal flow over the shallow topography. This results in more extreme relative vorticities and vertical velocities. The ageostrophic velocity in the filaments and meanders is restratifying, which leads to increased water mass transformation as the energy put in by the surface wind stress goes to turbulent mixing.

b. *Potential vorticity budget*

Following Marshall and Nurser (1992) and Thomas and Ferrari (2008), the potential vorticity q is modified by the divergence of the potential vorticity flux vector $\mathbf{J}$:

$$q_t = -\nabla \cdot \mathbf{J}, \tag{5}$$

where

$$\mathbf{J} = \mathbf{u}q + \nabla b \times \mathbf{F} - \omega_a D. \tag{6}$$

The first term in (6) represents advection, the second term represents frictional and body forces, and the third term is due to diapycnal mixing of buoyancy $D = -g\alpha_S D_S/\rho_0$, where $\omega_a = f_0\mathbf{k} + \nabla \times \mathbf{u}$ is the absolute vorticity. The advection term drops out when integrated over the closed domain, and so it reduces to a balance between frictional and diabatic potential vorticity fluxes in a steady state. We further break down the frictional potential vorticity flux at the surface into contributions from wind stress ($\mathbf{J}_w$) and vertical viscosity in the interior ($\mathbf{J}_g$):

$$\nabla b \times \mathbf{F}|_{z=0} \approx \mathbf{J}_w + \mathbf{J}_g, \tag{7}$$

where

$$\mathbf{J}_w = \frac{\tau_0 b_x}{\rho_0 \delta}\mathbf{k} \quad \mathbf{J}_g = \frac{\tau^g \cdot \nabla b}{\rho_0 \delta}\mathbf{k} = -\frac{\kappa_v \mathbf{v}_{gz} \cdot \nabla b}{\delta}\mathbf{k} \approx -\frac{\kappa_v (\nabla b)^2}{\delta f_0}\mathbf{k}. \tag{8}$$

It has been assumed for both terms that the frictional force is dominated by the vertical variation of the turbulent stress, that is, $\mathbf{F} \approx (\tau/\rho_0)_z\mathbf{k}$, and is distributed over the mixed layer depth δ. The viscous momentum flux in $\mathbf{J}_g$ is assumed to be dominated by the vertical diffusion of the geostrophic momentum, which is represented by the geostrophic stress $\tau^g = -\rho_0\kappa_v\mathbf{v}_{gz}$ and $\mathbf{v}_{gz}$ is the vertical derivative of the geostrophic velocity.

For a region with buoyant water along the coast and a surface-intensified geostrophic current, $b_x < 0$, $v_{gz} < 0$, and $\tau^g > 0$. The wind stress term $\mathbf{J}_w$ is positive at the surface, which leads to a decrease in potential vorticity from (5). For the surface-intensified current, the geostrophic stress $\mathbf{J}_g$ is negative. In the momentum equation, this negative stress is balanced by an offshore Ekman flow, which restratifies the front and leads to an increase in the potential vorticity (Thomas and Rhines 2002; Thomas and Ferrari 2008). This is the sense of the ageostrophic circulation shown in Fig. 7. The last term on the right-hand side of (6) is positive where D_S is positive (shown in Fig. 4c), leading to a decrease in b and the potential vorticity in regions of positive absolute vorticity.

The potential vorticity $\langle q \rangle$, where $\langle\ \rangle$ indicates the basin average, has been calculated for the standard case and the case without winds (Fig. 10a). The initial potential vorticity is slightly negative as a result of the initial lack of stratification and the negative contribution from the baroclinic term. Early in both calculations the potential vorticity increases but they diverge after a few days, when the winds have increased. The potential vorticity for the case with winds rapidly decreases to slightly negative $\langle q \rangle$ and remains there for the duration of the calculation. However, without winds, $\langle q \rangle$ continues to increase, rapidly at first and then more slowly for the final 15 days.

The frictional and diapycnal mixing terms have been calculated from the model terms in the momentum (for $\mathbf{F}$) and salinity (for D_S) equations and used to reproduce $\langle q \rangle$ (dashed lines in Fig. 10a).[2] The equilibrium balance of slightly negative $\langle q \rangle$ in the case with winds is the result of cancellation of generation by friction and destruction by mixing (Fig. 10b). For the case without winds, both terms are generally smaller than with winds, but the frictional term always exceeds the diapycnal mixing term, leading to the increase in potential vorticity. So even though the restratification by baroclinic instability in the absence of winds is approximately adiabatic, frictional effects are essential. The difference in the diabatic terms in Fig. 10b reflect the

[2] Some averaging is still required to derive the potential vorticity fluxes since the model uses a staggered C grid.

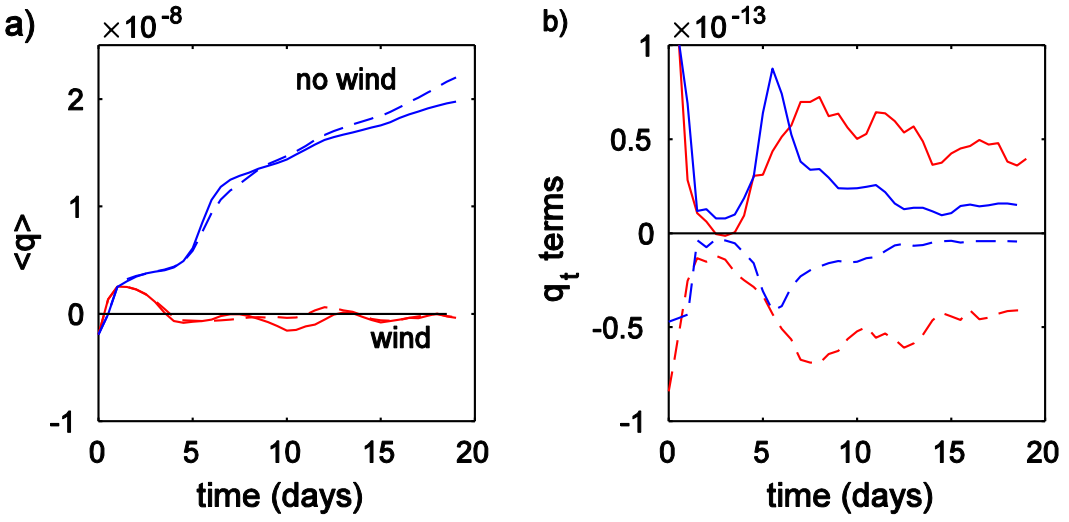

FIG. 10. Time evolution of (a) the basin-averaged potential vorticity [solid lines from the model, dashed lines from integration of terms in (b); s^{-3}] and (b) the frictional (solid) and mixing (dashed) contributions (s^{-4}). Red lines in (b) are for the case with $\tau = -0.2\,\mathrm{N\,m^{-2}}$ (run 1) and blue lines are for the case without winds (run 7).

increased water mass transformation rate for the case with winds (Fig. 5).

The potential vorticity budget, when combined with the buoyancy budget, can be used to provide a scaling for the eddy buoyancy flux. If it is assumed that the frictional potential vorticity flux is dominated by the vertical component of the geostrophic stress term and is balanced, on average, by the diapycnal mixing term, then

$$\left\langle \frac{\kappa_v (\nabla b)^2}{f_0 H} \right\rangle = \langle (f_0 + \zeta) D \rangle , \tag{9}$$

where H is the bottom depth. As shown in the following section, the geostrophic stress term will dominate the wind stress term for weak winds, and so this scaling is most appropriate in that limit.

A scatterplot of the meridional average of $-\nabla \cdot \overline{\mathbf{u}'S'}$ versus D_S (from Figs. 3d,b) in Fig. 11 shows that the eddy flux divergence scales nearly linearly with the diapycnal mixing rate. The slope of a linear regression is -1.7 with an R^2 of 0.85. The same calculation for each of the model runs in Table 1 gives a mean slope of -1.5 and a mean R^2 of 0.88 (and all values of R^2 fall between 0.84 and 0.92). This indicates that the eddy flux divergence scales linearly with the diapycnal mixing rate:

$$\nabla \cdot \overline{\mathbf{u}'b'} \propto D . \tag{10}$$

Combining these two budgets gives

$$\langle \overline{\mathbf{u}'b'} \rangle \propto \left\langle \frac{(\nabla_h b)^2 L H}{f_0 + \zeta} \frac{\kappa_v}{f_0 H^2} \right\rangle , \tag{11}$$

where L is the horizontal scale of the eddy flux divergence. This is essentially the same as the expression derived by Bachman and Taylor (2016) for a baroclinic current subject to strong vertical mixing in their small Richardson number limit if the lateral eddy buoyancy flux here is converted to their vertical eddy buoyancy flux via $\overline{w'b'} = \overline{u'b'}\,H/L$, and we interpret H/L as the isopycnal slope. Their formulation also did not explicitly include the wind stress or Ekman transport, consistent with the limit where the geostrophic stress dominates the wind stress. This scaling result differs from the scaling of Fox-Kemper et al. (2008) by the second term

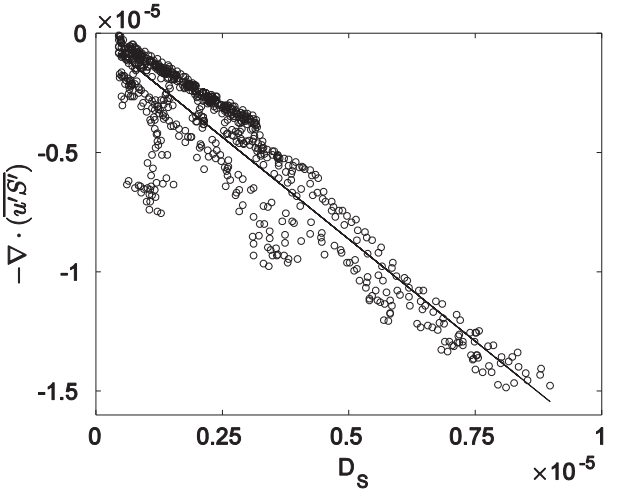

FIG. 11. Scatterplot of the eddy flux divergence vs the diapycnal mixing rate for run 1. These data points are limited to the upper 30 m in regions where the mixing exceeds 10% of its maximum mean value.

TABLE 1. Summary of three-dimensional model runs: wind stress τ, initial change in salinity across front ΔS, and average water mass transformation rate S^*.

Run	τ (N m^{-2})	ΔS (psu)	S^* (10^6 psu m^3 s^{-1})
1	−0.2	3	0.24
2	−0.1	3	0.13
3	−0.4	3	0.33
4	−0.6	3	0.44
5	−0.8	3	0.50
6	−1.0	3	0.59
7	0.0	3	0.01
8	−0.2	0.5	0.04
9	−0.2	1	0.07
10	−0.2	2	0.17
11	−0.2	4	0.30

on the right-hand side, which is the Ekman number, and by the presence of ζ in the denominator. While the Fox-Kemper et al. numerical evaluation provided an empirical-scale factor of approximately 0.06 for spin-down calculations, Bachman and Taylor (2016), and the present results, find a scale factor of $O(1)$ for forced/dissipative conditions. This difference is partially mitigated by $\kappa_v/f_0H^2 < 1$.

c. Parameter dependencies

Similar characteristics are produced over a wide range of wind stress and change in salinity across the front. Some basic scaling estimates are now developed for the magnitude of the potential vorticity flux terms and the resulting water mass transformation rate.

The case with $\tau = -0.2\,\mathrm{N\,m^{-2}}$ produces patches of stratified water along the frontal region with boundary layer depths of $O(25)$ m. A similar pattern is found for increasing wind stress and also for different values of the change in salinity across the front. The average depth of the planetary boundary layer where it does not reach the bottom is shown in Fig. 12 as a function of wind stress with $\Delta S = 3$ psu. For all values of wind stress, the boundary layer thickness is $O(25)$. This balance between wind stress working to steepen isopycnals and eddy fluxes working to flatten isopycnals, such that increases in the wind stress are largely offset by increases in the eddy fluxes, is similar to the eddy saturation found in models of the Antarctic Circumpolar Current (Munday et al. 2013). The vertical viscosity diagnosed in these regions increases approximately as the frictional velocity assuming a constant boundary layer depth: $\kappa_v \propto u^*\delta = (\tau/\rho_0)^{1/2}\delta$ (Fig. 12). This is consistent with the finding that the planetary boundary layer depth δ does not scale as the Ekman layer thickness, which, if it did, would result in $\kappa_v \propto \tau$. Although the wind stress does not significantly influence the thickness of the stratified patches of water, it does influence their extent. The

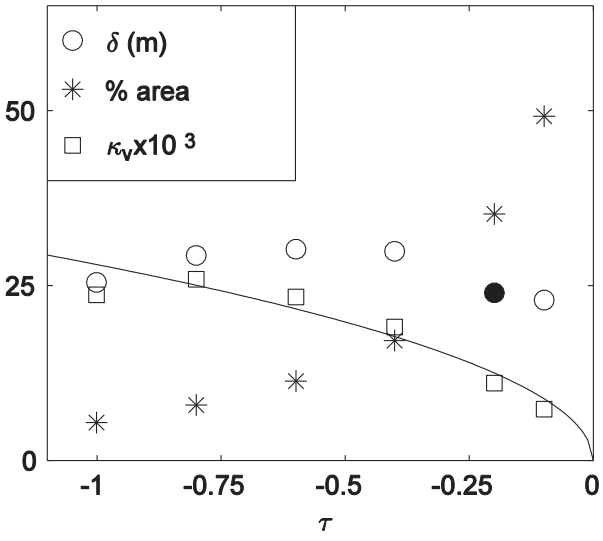

FIG. 12. Average boundary layer thickness (circles), percent of the domain covered by stratified flow (asterisks), and $10^3\kappa_v$ averaged over the stratified regions (squares) as a function of wind stress with $\Delta S = 3$ psu. The solid line is proportional to $\tau^{1/2}$.

percent of the model domain that is stratified (defined as regions where the boundary layer thickness is less than the bottom depth) decreases from approximately 50% for $\tau = -0.1\,\mathrm{N\,m^{-2}}$ to less than 10% for $\tau = -1\,\mathrm{N\,m^{-2}}$ (Fig. 12).

Examples of the surface salinity and the planetary boundary layer thickness for $\tau = -0.8\,\mathrm{N\,m^{-2}}$ are shown in Fig. 13. Most of the domain is unstratified but there are small patches of shallow boundary layers with spatial scales of $O(10)$ km. These are found in regions where buoyant water has been advected offshore (along $x = 80$ km) and in regions of strong fronts (along $x = 60$ km). These regions of stratified water are produced by two distinct processes. The geostrophic stress term acts to restratify the fluid in regions of strong fronts. The wind stress can also restratify the flow in regions where the zonal buoyancy gradient is positive, such as the meanders extending offshore in Fig. 13, although integrated over the whole domain this term is always destratifying.

The domain average of the potential vorticity flux at the surface due to these terms is shown as a function of wind stress in Fig. 14a. The geostrophic stress contribution $\mathbf{J}_g$ is always negative and increases approximately as $\tau^{1/2}$ (circles). The sign convention is such that negative surface potential vorticity flux leads to an increase in the potential vorticity q from (5). The average wind stress term $\mathbf{J}_w$ is always positive and scales linearly with τ (squares). The regions of negative contribution resulting from the wind stress acting on regions of positive buoyancy gradient $\mathbf{J}_w$ increase with increasing wind stress (triangles) but are always much less than the geostrophic stress term.

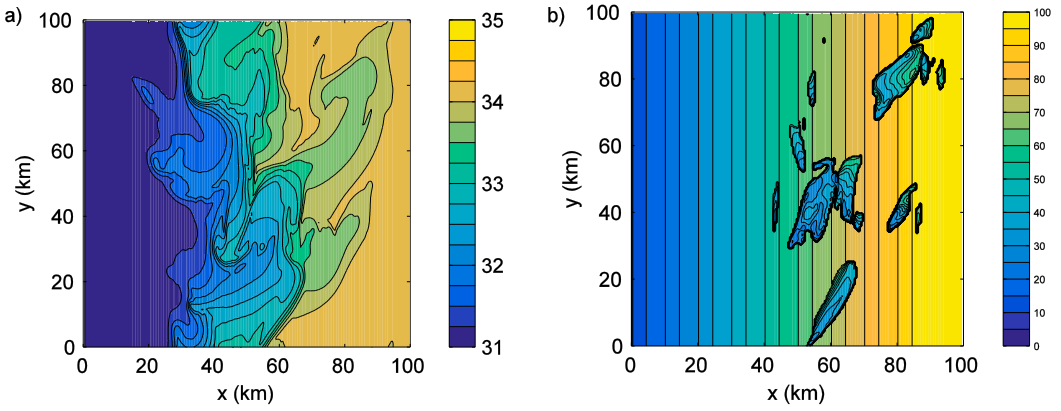

FIG. 13. Snapshot on day 15 of (a) sea surface salinity (psu) and (b) planetary boundary layer thickness (m) for a case with $\tau = -0.8\,\mathrm{N\,m^{-2}}$ (run 5).

The potential vorticity flux at the surface due to the wind stress $\mathbf{J}_w = \tau b_x/(\rho_0\delta)\mathbf{k}$ is linear in b and τ is uniform, so it can be integrated over the domain to get an estimate for the average PV flux due to the wind:

$$\langle J_w \rangle = -\frac{g\tau\alpha_S \Delta S}{\rho_0^2 \delta L_x}, \tag{12}$$

where L_x is the domain width (this is the domain-averaged flux, so a wider basin for the same ΔS gives a lower average flux). This estimate is given in Fig. 14a by the solid line tracking the square symbols. There is no equivalent estimate for the positive contribution due to the wind stress, which will depend on the stability characteristics of the front and the extent of meandering.

It is difficult to derive a general expression for the geostrophic stress term $\mathbf{J}_g$, but some progress can be made with assumptions guided by the model results. The geostrophic stress term is largest in the regions of stratified flow where it was found that the vertical viscosity coefficient scales as $(\tau/\rho_0)^{1/2}\delta$. The vertical shear of the geostrophic velocity is related to the buoyancy gradient as $\mathbf{v}_{gz} = \mathbf{k} \times \nabla b/f_0$. This gives rise to the nonlinearity $(\nabla b)^2$ in (8). If it is assumed that this term scales as $(\alpha_S \Delta S)^2$, then a parameter dependency for the geostrophic stress can be estimated as

$$\langle J_g \rangle \propto |\tau|^{1/2} \Delta S^2, \tag{13}$$

with an unknown scaling factor. The geostrophic stress also likely depends on other parameters, such as f_0, the bottom depth, and the bottom slope. Calculations with larger and smaller f_0, or different bottom slopes and depths, produce different values of $\langle J_g \rangle$, so this scaling relationship is not complete. Nonetheless, the scaling for the present model configuration indicates that the PV flux due to the geostrophic stress term should increase as $\tau^{1/2}$, which is indicated in Fig. 14a by the solid line tracking the circles.

A wider test of (12) and (13) is shown in Fig. 14b for a range of wind stress $\tau = -0.1, -0.2, -0.4, -0.6, -0.8$, and $-1.0\,\mathrm{N\,m^{-2}}$ and $\Delta S = 0.5, 1, 2, 3$, and 4 psu (see Table 1). The scaling estimates compare well with that diagnosed from the model over the entire range of parameter space.

Because the geostrophic stress term increases as $\tau^{1/2}$ and the wind stress term increases as τ, it is expected that the geostrophic stress will dominate for weak to moderate wind stresses, and the wind stress will dominate for very strong wind stresses. This will result in the diapycnal mixing term in the potential vorticity equation changing from negative (decreasing $\langle q \rangle$) for weak winds to positive (increasing $\langle q \rangle$) for strong winds. The basin average of this mixing term $\langle [(f_0 + \zeta)D]_z \rangle$ is shown in Fig. 14c as a function of wind stress and the change in salinity across the front. Consistent with Fig. 14a, the mixing term is negative for $|\tau| < 0.6\,\mathrm{N\,m^{-2}}$ and positive for $|\tau| > 0.6\,\mathrm{N\,m^{-2}}$. While the value of the wind stress at this transition likely depends on many parameters, such as ΔS, f_0, and bottom topography, the existence of such a transition is probably robust. The mixing term becomes increasingly negative with increasing change in salinity across the front. This is also consistent with (12) and (13) because the geostrophic stress term increases as ΔS^2, while the wind stress term increases as ΔS.

The diapycnal mixing rate is given by the area integral of the vertical diffusive flux $S^* = \int \kappa_S S_z \mathcal{H}(D_S)\, dA$. For the vertical structure function used in the KPP model, the vertical average of the vertical mixing coefficient is approximately $\kappa_S \approx \kappa(|\tau|/\rho_0)^{1/2}\delta/6$, where $\kappa = 0.4$ is the Von Kármán constant. If it is assumed that $S_z \propto \Delta S/\delta$, then the diapycnal mixing rate should scale as

$$S^* \propto (\kappa/6)\Delta S(|\tau|/\rho_0)^{1/2} A, \tag{14}$$

where A is the horizontal area over which the baroclinic zone extends. For all calculations here, this is $O(10^9)\,\mathrm{m^2}$. There is an additional scale factor of less than 1 since the

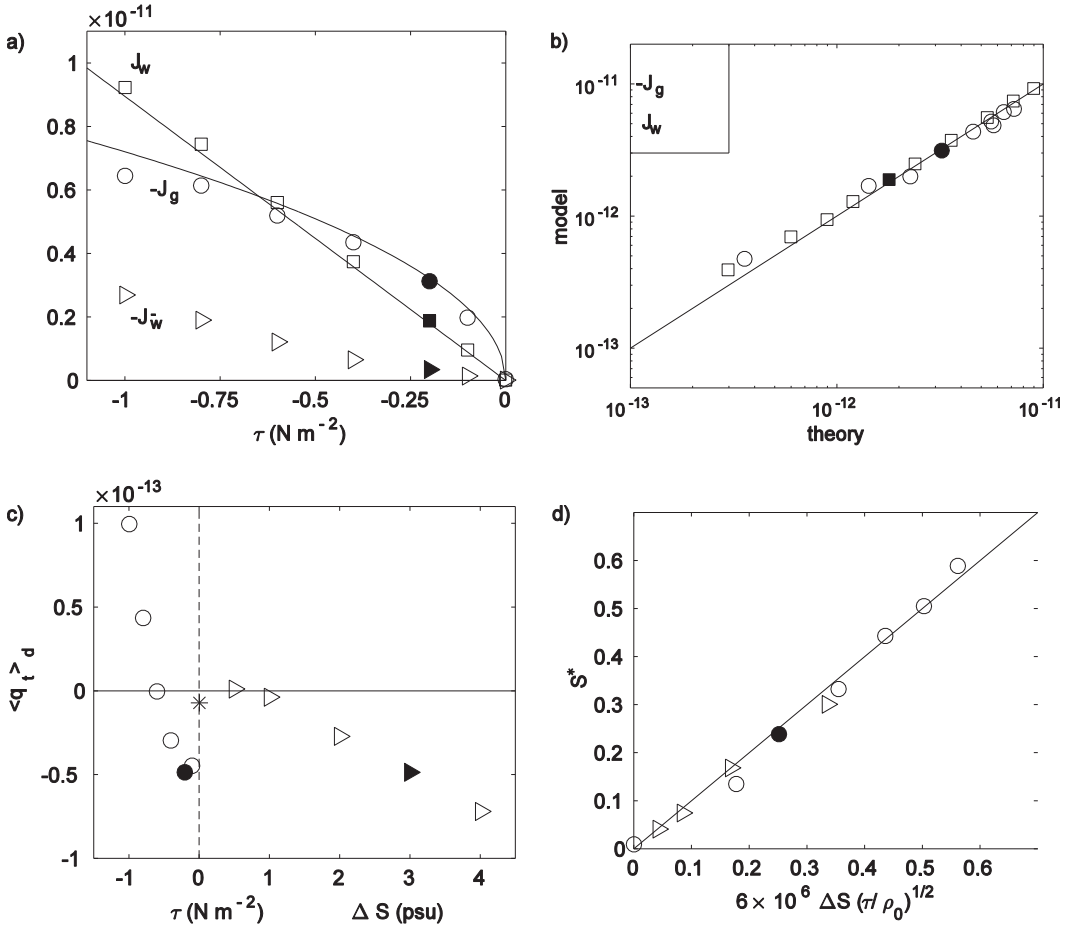

FIG. 14. (a) Basin-averaged potential vorticity flux due to the (negative of the) geostrophic stress (circles), wind stress (squares), and negative regions due to wind stress (triangles) ($\mathrm{m\,s^{-4}}$). (b) Comparison between potential vorticity fluxes diagnosed from the model and the scaling in (12) and (13) ($\mathrm{m\,s^{-4}}$). (c) Basin-averaged contribution to the potential vorticity due to diapycnal mixing $\langle[(f_0 + \zeta)D]_z\rangle$. Circles correspond to variations in wind stress (with $\Delta S = 3$ psu), and triangles correspond to variations in the change in salinity across the front (with $\tau = -0.2\,\mathrm{N\,m^{-2}}$). The asterisk is for zero wind stress. (d) Basin-integrated water mass transformation rate (10^6 psu $\mathrm{m^3\,s^{-1}}$) diagnosed from the model compared to scaling $6 \times 10^6\,\Delta S\tau^{1/2}$. The solid symbols are for the standard case with $\tau = -0.2\,\mathrm{N\,m^{-2}}$.

change in salinity in the vertical over the boundary layer thickness δ will always be less than ΔS. Nonetheless, the parameter dependence predicted by (14) compares well with the transformation rate S^* diagnosed from the model runs with a constant of proportionality of $6 \times 10^6\,\mathrm{m^2}$ (Fig. 14c).

Although the wind stress term exceeds the geostrophic stress term, this does not require that the destratification due to the advection of buoyancy by the Ekman transport exceed the restratification due to horizontal eddy fluxes. In fact, the mean buoyancy budget for the case with very strong winds ($\tau = -1\,\mathrm{N\,m^{-2}}$) looks much like that in Fig. 3 where restratification by eddy fluxes scales linearly with the vertical diffusion (not shown). The horizontal integral of the buoyancy tendency due to diapycnal mixing at the surface was calculated and binned according to the value of the absolute vorticity (Fig. 15a). Diapycnal mixing reduces the surface buoyancy for $\zeta < 0$ (stable stratification, increases surface salinity). Only at very strong positive relative vorticities, where the vertical density gradient is positive, does mixing increase the surface buoyancy. Despite the fact that the diapycnal mixing is, on average, decreasing the stratification, vertical mixing of buoyancy leads to an overall increase in the potential vorticity budget. This is shown by the area integral of the contribution of diapycnal mixing to the potential vorticity tendency (Fig. 15b, where it has been assumed that this mixing is distributed over the mixed layer depth δ). This results from regions of negative relative vorticity reducing and eventually

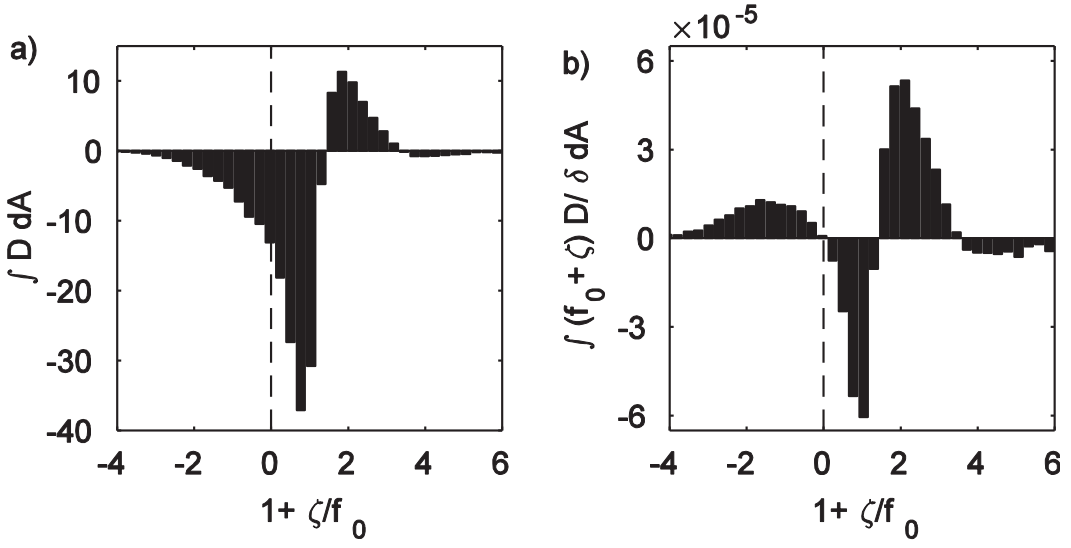

FIG. 15. Histogram of the spatial integral of change in (a) buoyancy ($m^3 s^{-3}$) and (b) potential vorticity ($m^2 s^{-4}$) at the surface due to vertical mixing binned into the absolute vertical vorticity at the surface for the case with $\tau = -1\,N\,m^{-2}$ (run 6).

changing the sign of the potential vorticity tendency compared to the buoyancy tendency (recall that D is multiplied by the absolute vorticity in the q tendency equation) and the large positive relative vorticity increasing the influence of the positive vertical density gradient regions. The total integrated potential vorticity tendency is $1.7 \times 10^{-4}\,m^2\,s^{-4}$. The contribution where $1 + \zeta/f_0 < 0$ is $1.1 \times 10^{-4}\,m^2\,s^{-4}$, and the contribution where $1 + \zeta/f_0 > 1$ is $1.4 \times 10^{-4}\,m^2\,s^{-4}$. These regions of increasing potential vorticity tendency are counteracted in regions where $-f_0 < \zeta < 0$ by $-0.8 \times 10^{-4}\,m^2\,s^{-4}$. Thus, vertical mixing can both decrease the vertical stratification and increase the potential vorticity because of the influence of the relative vorticity.

5. Summary

A series of calculations with an idealized numerical model and scaling have been used to explore the interaction of downfront winds with baroclinic instability in buoyant coastal plumes. The primary balance in the buoyancy equation is between restratification by lateral eddy fluxes and destratification by vertical mixing and, to a lesser extent, mean advection, for all values of wind stress and buoyancy gradients tested. The resulting water mass transformation takes place primarily along the anticyclonic side of mesoscale meanders. The onshore Ekman transport is not generally sufficient to result in positive vertical density gradients in the vicinity of the front, but it does provide a large-scale frontogenetic flow that maintains a baroclinic gradient tens of kilometers wide, which is susceptible to baroclinic instability. The submesoscale fronts that result from this instability create the regions where water mass transformation takes place through vertical mixing forced by the surface wind stress. The presence of the coast enhances this effect and results in more intense vertical motions and relative vorticities compared to a similar downfront wind in the absence of a coast. It is the combination of baroclinic instability and downfront winds that results in significant water mass transformation.

With downfront winds, the basin-averaged potential vorticity $\langle q \rangle$ is nearly zero. For weak to moderate winds, this results from a balance between vertical mixing, which decreases $\langle q \rangle$, and geostrophic stress, which increases $\langle q \rangle$. For strong winds, the wind stress exceeds the geostrophic stress, resulting in a decrease in $\langle q \rangle$ that is balanced by an increase in $\langle q \rangle$ due to vertical mixing in regions of large (positive and negative) relative vorticity. In the absence of winds the geostrophic stress term dominates and the fluid rapidly restratifies. By combining the $\langle q \rangle$ budget with the buoyancy budget an estimate is derived for the eddy buoyancy flux appropriate for weak winds that agrees with the recent theoretical result of Bachman and Taylor (2016). A scaling is also developed for the magnitude of the surface potential vorticity flux due to winds, due to the geostrophic stress, and for the water mass transformation rate. Each of these scaling estimates compares well with results diagnosed from a series of numerical model calculations.

These results highlight the role of downfront winds in driving water mass transformation in buoyant coastal

plumes. However, the details are more complex than the simple, two-dimensional, linear expectation that mixing is driven by the Ekman flux of dense water over light water. Consideration of the third dimension, and the mechanism of baroclinic instability, changes the dominant balance in the density equation and greatly enhances the net water mass transformation compared to the two-dimensional case.

Acknowledgments. This study was supported by NSF Grants OCE-1433170 (MAS) and OCE-1459677 (LNT). Comments and suggestions by two anonymous reviewers helped to clarify the presentation.

REFERENCES

Allen, J. S., and P. A. Newburger, 1996: Downwelling circulation on the Oregon continental shelf. Part I: Response to idealized forcing. *J. Phys. Oceanogr.*, **26**, 2011–2035, doi:10.1175/1520-0485(1996)026<2011:DCOTOC>2.0.CO;2.

Bachman, S. D., and J. R. Taylor, 2016: Numerical simulations of the equilibrium between eddy-induced restratification and vertical mixing. *J. Phys. Oceanogr.*, **46**, 919–935, doi:10.1175/JPO-D-15-0110.1.

Batifoulier, F., P. Lazure, and P. Bonneton, 2012: Poleward coastal jets induced by westerlies in the Bay of Biscay. *J. Geophys. Res.*, **117**, C03023, doi:10.1029/2011JC007658.

Boccaletti, G., R. Ferrari, and B. Fox-Kemper, 2007: Mixed layer instabilities and restratification. *J. Phys. Oceanogr.*, **37**, 2228–2250, doi:10.1175/JPO3101.1.

D'Asaro, E., C. M. Lee, L. Rainville, R. Harcourt, and L. N. Thomas, 2011: Enhanced turbulence and energy dissipation at ocean fronts. *Science*, **332**, 318–332, doi:10.1126/science.1201515.

Dickson, R. R., J. Meincke, S.-A. Malmberg, and A. J. Lee, 1988: The "Great Salinity Anomaly" in the northern North Atlantic, 1968–1982. *Prog. Oceanogr.*, **20**, 103–151, doi:10.1016/0079-6611(88)90049-3.

Fichefet, T., C. Poncin, H. Goosse, P. Huybrechts, I. Janssens, and H. L. Truet, 2003: Implications of changes in freshwater flux from the Greenland Ice Sheet for the climate of the 21st century. *Geophys. Res. Lett.*, **30**, 1911, doi:10.1029/2003GL017826.

Fox-Kemper, B., R. Ferrari, and R. Hallberg, 2008: Parameterization of mixed layer eddies. Part I: Theory and diagnosis. *J. Phys. Oceanogr.*, **38**, 1145–1165, doi:10.1175/2007JPO3792.1.

Garrett, C. J. R., and J. W. Loder, 1981: Dynamical aspects of shallow sea fronts. *Philos. Trans. Roy. Soc. London*, **A302**, 563–581, doi:10.1098/rsta.1981.0183.

Gula, J., M. J. Molemaker, and J. C. McWilliams, 2014: Submesoscale cold filaments in the Gulf Stream. *J. Phys. Oceanogr.*, **44**, 2617–2643, doi:10.1175/JPO-D-14-0029.1.

Harden, B. E., I. A. Renfrew, and G. N. Petersen, 2011: A climatology of wintertime barrier winds off southeast Greenland. *J. Climate*, **24**, 4701–4717, doi:10.1175/2011JCLI4113.1.

Hoskins, B. J., 1974: The role of potential vorticity in symmetric stability and instability. *Quart. J. Roy. Meteor. Soc.*, **100**, 480–482, doi:10.1002/qj.49710042520.

——, 1982: The mathematical theory of frontogenesis. *Annu. Rev. Fluid Mech.*, **14**, 131–151, doi:10.1146/annurev.fl.14.010182.001023.

Jungclaus, J. H., H. Haak, M. Esch, E. Roeckner, and J. Marotzke, 2006: Will Greenland melting halt the thermohaline circulation? *Geophys. Res. Lett.*, **33**, L17708, doi:10.1029/2006GL026815.

Large, W. G., J. C. McWilliams, and S. C. Doney, 1994: Oceanic vertical mixing: A review and a model with a nonlocal boundary layer parameterization. *Rev. Geophys.*, **32**, 363–403, doi:10.1029/94RG01872.

Magaldi, M. G., T. M. Ozgokmen, A. Griffa, and M. Rixen, 2010: On the response of a turbulent coastal buoyant current to wind events: The case of the western Adriatic Current. *Ocean Dyn.*, **60**, 93–122, doi:10.1007/s10236-009-0247-9.

Mahadevan, A., A. Tandon, and R. Ferrari, 2010: Rapid changes in mixed layer stratification driven by submesoscale instabilities and winds. *J. Geophys. Res.*, **115**, C03017, doi:10.1029/2008JC005203.

Marshall, J., and A. J. G. Nurser, 1992: Fluid dynamics of oceanic thermocline ventilation. *J. Phys. Oceanogr.*, **22**, 583–595, doi:10.1175/1520-0485(1992)022<0583:FDOOTV>2.0.CO;2.

——, C. Hill, L. Perelman, and A. Adcroft, 1997: Hydrostatic, quasi-hydrostatic, and non-hydrostatic ocean modeling. *J. Geophys. Res.*, **102**, 5733–5752, doi:10.1029/96JC02776.

McWilliams, J. C., J. Gula, J. Molemaker, L. Renault, and A. F. Shchepetkin, 2015: Filament frontogenesis by boundary layer turbulence. *J. Phys. Oceanogr.*, **45**, 1988–2005, doi:10.1175/JPO-D-14-0211.1.

Moffat, C., and S. Lentz, 2012: On the response of a buoyancy plume to downwelling-favorable wind stress. *J. Phys. Oceanogr.*, **42**, 1083–1098, doi:10.1175/JPO-D-11-015.1.

Munday, D. R., H. L. Johnson, and D. P. Marshall, 2013: Eddy saturation of equilibrated circumpolar currents. *J. Phys. Oceanogr.*, **43**, 507–532, doi:10.1175/JPO-D-12-095.1.

Nagai, T., A. Tandon, and D. L. Rudnick, 2006: Two-dimensional ageostrophic secondary circulation at ocean fronts due to vertical mixing and large-scale deformation. *J. Geophys. Res.*, **111**, C09038, doi:10.1029/2005JC002964.

Niiler, P. P., 1969: On the Ekman divergence in an oceanic jet. *J. Geophys. Res.*, **74**, 7048–7052, doi:10.1029/JC074i028p07048.

Oguz, T., D. Macias, and J. Tintore, 2015: Ageostrophic frontal processes controlling phytoplankton production in the Catalano-Balearic Sea (western Mediterranean). *PLOS One*, **10**, e0129045, doi:10.1371/journal.pone.0129045.

Stern, M. E., 1965: Interaction of a uniform wind stress with a geostrophic vortex. *Deep-Sea Res. Oceanogr. Abstr.*, **12**, 355–367, doi:10.1016/0011-7471(65)90007-0.

Thomas, L. N., 2005: Destruction of potential vorticity by winds. *J. Phys. Oceanogr.*, **35**, 2457–2466, doi:10.1175/JPO2830.1.

——, and P. B. Rhines, 2002: Nonlinear stratified spin-up. *J. Fluid Mech.*, **473**, 211–244, doi:10.1017/S0022112002002367.

——, and R. Ferrari, 2008: Friction, frontogenesis, and the stratification of the surface mixed layer. *J. Phys. Oceanogr.*, **38**, 2501–2518, doi:10.1175/2008JPO3797.1.

——, and J. R. Taylor, 2010: Reduction of the useable wind-work on the general circulation by forced symmetric instability. *Geophys. Res. Lett.*, **37**, L18606, doi:10.1029/2010GL044680.

Thompson, L., 2000: Ekman layers and two-dimensional frontogenesis in the upper ocean. *J. Geophys. Res.*, **105**, 6437–6451, doi:10.1029/1999JC900336.

Whitney, M. M., and R. W. Garvine, 2005: Wind influence on a coastal buoyant outflow. *J. Geophys. Res.*, **110**, C03014, doi:10.1029/2003JC002261.